Revision 1

The formation of marine red beds and iron cycling on the Mesoproterozoic North China Platform

DONGJIE TANG*[1, 2], JIANBAI MA[3], XIAOYING SHI[1, 3], MAXWELL LECHTE[4], AND XIQIANG ZHOU[5]

[1]State Key Laboratory of Biogeology and Environmental Geology, China University of Geosciences (Beijing), Beijing 100083, China

[2]Institute of Earth Sciences, China University of Geosciences (Beijing), Beijing 100083, China

[3]School of Earth Sciences and Resources, China University of Geosciences (Beijing), Beijing 100083, China

[4]Department of Earth and Planetary Sciences, McGill University, 3450 University Street, Montréal, QC H3A 0E8, Canada

[5]Key Laboratory of Petroleum Resources Research, Institute of Geology and Geophysics, Chinese Academy of Sciences, Beijing 100029, China

*Corresponding author. E-mail: dongjtang@126.com (D. Tang), Tel.: +86 10 82323199.

ABSTRACT

Marine red beds (MRBs) are common in sedimentary records, but their genesis and environmental implications remain controversial. Genetic models proposed for MRBs variably invoke diagenetic or primary enrichments of iron, with vastly different implications for the redox state of the contemporaneous water column. The Xiamaling Formation (ca. 1.4

Ga) in the North China Platform hosts MRBs that offer insights into the iron cycling and redox conditions during the Mesoproterozoic Era. In the Xiamaling MRBs, well-preserved, nanometer-sized flaky hematite particles are randomly dispersed in the clay (illite) matrix, within the pressure shadow of rigid detrital grains. The presence of hematite flake aggregates with multiple face-to-edge ("cardhouse") contacts indicates that the hematite particles were deposited as loosely-bound, primary iron oxyhydroxide flocs. No greenalite or other ferrous iron precursor minerals have been identified in the MRBs. Early diagenetic ankerite concretions hosted in the MRBs show non-zero I/(Ca+Mg) values and positive Ce anomalies (>1.3), suggesting active redox cycling of iodine and manganese and therefore the presence of molecular oxygen in the porewater and likely in the water column during their formation. These observations support the hypothesis that iron oxyhydroxide precipitation occurred in moderately oxygenated marine waters above storm wave base (likely <100 m). Continentally-sourced iron reactivated through microbial dissimilatory iron reduction and distal hydrothermal fluids may have supplied Fe(II) for the iron oxyhydroxide precipitation. The accumulation of the Xiamaling MRBs may imply a slightly increase of seawater oxygenation and the existence of long-lasting adjacent ferruginous water mass.

Keywords: marine red beds, hematite, ferruginous, dissimilatory iron reduction, Xiamaling Formation, oxygenation

INTRODUCTION

Marine red beds are sedimentary successions deposited from seawater that are enriched in iron oxides, imparting a characteristic red color (e.g., Hu et al. 2012). Although MRBs contain less iron (typically containing Fe <15 wt%) and simpler iron mineral assemblages than that of iron formations, ancient MRBs have been widely used as important tracers for surface-system redox conditions through geological time. However, the iron cycling processes responsible for the deposition of MRBs—and thus their paleoenvironmental significance—remain elusive.

The enrichment of iron oxides in MRBs has been variably ascribed to detrital, primary, early or late diagenetic origins (e.g. Franke and Paul 1980; Hu et al. 2006, 2012; Song et al. 2017; Liu et al. 2019a; Zou et al. 2019), and each of these hypotheses has vastly different implications for reconstructing ancient seawater chemistry. Detritally sourced iron oxide is responsible for iron enrichment in some marine sediments (e.g., Franke and Paul 1980), but the observation of MRBs intercalated with iron-poor turbidites suggests that the supply of terrestrial iron oxides is not the controlling factor for MRB deposition (Hu et al. 2012). More recent interpretations suggest that the oxidation of Fe(II) in a ferruginous seawater column may have been important in the deposition of MRBs, such as the abiotic oxidation of Fe(II) following ocean anoxic events (Song et al. 2017). This hypothesis requires an anoxic event to accumulate Fe(II) in seawater, followed by marine oxygenation to oxidize Fe(II) and precipitate poorly crystalline hydrous ferric oxide phases that can be converted to hematite during diagenesis (Song et al. 2017). However, the duration of red bed deposition could be in the order of millions of years (Hu et al. 2012): the Fe(II) accumulated during ocean anoxic events would be rapidly exhausted during marine oxygenation because of short residence time of Fe(II) in oxygenated seawater (100–200 yr, Johnson et al. 1997). Alternatively, seawater Fe(II) oxidation could have been microbially-mediated (Préat et al. 2008); the activity of microaerobic Fe(II)-oxidizing bacteria near the water–sediment interface has been suggested as the major cause for iron oxide enrichment in a number of Phanerozoic marine limestones (Mamet and Préat 2006). Early diagenetic origin is argued as the model for some carbonate MRBs, which suggests highly oxic, oligotrophic, and probably low-productivity seawater conditions (e.g., Hu et al. 2006). The post-depositional oxidation of Fe(II)-bearing minerals is also proposed as an important model for the genesis of continental red beds (e.g., Van Houten 1973) and MRBs (e.g., Galloway 1922). Finally, recent research suggests that Precambrian sedimentary ferric iron oxides may represent the post-depositional replacement of precursor iron mineral phases such as ferrous-ferric iron hydroxy salts (green rust; e.g. Halevy et al. 2017) or ferrous iron silicates (greenalite; e.g. Rasmussen et al. 2016). In sum, no genetic model for MRBs has been universally accepted at present.

The lack of a widely accepted genetic mechanism for MRBs further complicates our understanding of the chemical evolution of the Earth's oceans and atmosphere. Recent studies suggest that analyzing micro- to ultra-scopic fabrics of iron-bearing sedimentary rocks could provide valuable information on the origin and diagenetic evolution of sedimentary iron minerals (e.g., Lin et al. 2019; Rasmussen et al. 2019). Here, we apply this technology to analyze the red beds found in the Mesoproterozoic Xiamaling Formation (*ca.* 1.40–1.35 Ga), North China, which overlie chamosite and siderite-rich iron formations (Canfield et al. 2018; Tang et al. 2018) and are interpreted to have been deposited in a marine environment below storm wave base due to the general lack of wave-agitated depositional structures (Wang et al. 2017). Revealing the genesis of the MRBs may be important in reconstructing the highly debated paleoredox evolution of Mesoproterozoic seawater from iron formation-deposition to MRB-deposition during the enigmatic Mesoproterozoic Era (e.g., Poulton et al. 2010; Planavsky et al. 2011; Lyons et al. 2014; Sperling et al. 2014; Hardisty et al. 2017), which may have influenced the evolution of complex eukaryotes (e.g., Anbar and Knoll 2002; Planavsky et al. 2014).

GEOLOGICAL SETTING

We studied the Xiamaling Formation MRBs near the Zhaojiashan and Jizhentun villages in the Huailai–Xiahuayuan region (Hebei Province; Fig. 1a and b). In the study areas, the

Xiamaling Formation is dominantly composed of dark shales and siltstone, and can be subdivided into four members (Member I to IV) in ascending order. These units are interpreted to have constituted a large transgressive-regressive cycle, reaching peak transgression in Member III (Fig. 1c; Zhang et al. 2015a, 2016; Tang et al. 2017, 2018; Wang et al. 2017). Based on the high-precision zircon ages of 1384.4±1.4 and 1392.2±1.0 Ma from the middle part (Zhang et al. 2015a) and the zircon and baddeleyite ages of 1345±12 and 1353±14 Ma from the diabase sills in the upper part (Zhang et al. 2009), the duration of the Xiamaling Formation is well constrained between ~1.40 and ~1.35 Ga (Tang et al. 2018). The MRBs studied in this study occur in Member II and consist of three lithological units. The lower unit is characterized by gray to green, chamosite-rich, fine-grained sandstone and siltstone with some siderite-rich beds (Fig. 2a–d), which were formed through dissimilatory iron reduction of Fe-hydroxides precipitated from ferruginous seawater (Canfield et al. 2018; Tang et al. 2018). The middle unit consists of alternating red and green shales with ankerite concretions in the lower part and green shales in the upper part (Fig. 2e–g). The upper unit comprises mainly dark to black, organic-rich shales with carbonate concretions (Fig. 2h).

The fine-grained sandstones and siltstones of the lower Member II display well-developed laminations without recognizable wave-agitated structures or cross-bedding, likely indicative of a deposition in deep subtidal environment below fair-weather wave base (>25 m, Tang et al. 2017). In the shales of the middle to upper units, tiny grain size and no wave-agitated structures suggest the deepening of seawater and depositional environments below storm wave base (likely >100 m, Zhang et al. 2016, 2017).

Rocks in the Xiamaling Formation are well preserved and the organic matter preserved in this formation are thermally immature to early thermally mature, which shows that this formation has undergone a relatively low thermal evolution with burial temperatures of ≤90°C (Luo et al. 2015; Zhang et al. 2015a). In addition, a study of the Xiamaling chamosite polytypes has suggested a burial depth of <2000 m (Ryan and Reynolds Jr. 1996), corresponding to a burial temperature of <80°C (Tang et al. 2017). The study of biomarkers extracted from the Xiamaling black shale also indicates a low thermal maturity in the early to middle oil window, and that the organic matter was primarily derived from prokaryotes, with cyanobacteria as the major biomass (Luo et al. 2015).

SAMPLES AND METHODS

Samples analyzed in this study were collected from the Member II of the Xiamaling Formation along freshly exposed road cuts near Zhaojiashan (40°28'27.40"N, 115°23'30.78"E) and Jizhentun (40°28′12.16″N, 115°16′10.50″E), Hebei Province, North China (Fig. 1). Collected samples were cut into chips and only the fresh, central parts of the samples were used for mineralogical and geochemical analyses. For geochemical analyses, fresh sample chips were cleaned, dried, and then ground into powders (~200 mesh) in an agate mortar avoiding any metal contact.

Petrographic analysis was conducted on thin sections with a Stereo Discovery V20 microscope for large scope and a Zeiss Axio Scope A1 microscope for high magnification. Ultra-structures were investigated on argon ion milling chips using a Zeiss Supra 55 field emission scanning electron microscope (FESEM) under 20 kV accelerating voltage with a working distance of ~15 mm, in the FESEM Laboratory, China University of Geosciences (Beijing). Secondary electron imaging detector was used to characterize topographic features, and an AsB detector was used to reveal compositional difference (backscattered electron, BSE, image). Samples were coated with ~8 nm thick carbon for electric conduction before analysis.

In order to produce smooth sample surfaces for electron microscopy, ion milling was conducted in the FESEM Laboratory, China University of Geosciences (Beijing) with

GATAN Ilion 697 ion mills. Milled surfaces were mechanically polished using successively finer grit (down to 1 μm grit size) and were then milled for two hours at 6 kV and a beam incident angle of 0°. This approach produced smooth surfaces for later examination by FESEM, energy dispersive X-ray spectrometer (EDS) and electron backscatter diffraction (EBSD).

Element concentrations of micron-sized spots were quantitatively analyzed by an Oxford EDS connected to the FESEM, operated at 20 kV with a working distance of ~15 mm and beam diameter of ~2 μm, in the FESEM Laboratory, China University of Geosciences (Beijing). Minerals as well as synthetic phases (MINM25-53) were used as reference standards. Duplicate analyses of individual points showed analytical error less than 3%.

EBSD measurements were carried out in the FESEM Laboratory, China University of Geosciences (Beijing) using a Zeiss SUPRA 55 FESEM with an Oxford NordlysNano EBSD acquisition camera. The measurements were collected using an accelerating voltage of 20 kV, 200 nA beam current, and a working distance of ~25 mm. The sample surface was tilted 70° relative to horizontal to enlarge beam-specimen activation surface so that EBSD signal can be enhanced. Diffraction patterns were manually collected, and automatically indexed in real-time using the AZtec software from the HKL Technology, Oxford Instruments. Six to eight Kikuchi bands were included for the fitting algorithm. Only measurements with mean angular deviation (MAD) values below 1.0° were accepted for analyses, and the indexing rate is about 80%.

Twenty bulk rock powder samples were chosen for X-ray diffraction analysis. The samples were scanned after air-drying. The powder slides were scanned from 4° to 70° with a step size of 0.02° 2θ and a scan speed of 1°/min, using nickel filter copper radiation in a SmartLab X-Ray Diffractometer at China University of Geosciences (Beijing).

For I/(Ca+Mg) analyses of ankerite concretion samples, ~5 mg of sample powders below 200 mesh were rinsed 4 times with 18.25 MΩ Milli-Q (MQ) water to remove clay minerals (Tang et al. 2017) and any potential soluble salts. After drying, the samples were ground into smaller and more homogenized powders in an agate mortar, and then weighed. Nitric acid (3%) was added for dissolution and then centrifuged to obtain supernatant. For calcium (Ca) and magnesium (Mg) analyses, 0.2 mL supernatant was used and then diluted to 1:50,000 with 3% HNO_3 before analysis. Ca and Mg concentrations were measured using a PerkinElmer NexION 300Q Inductively Coupled Plasma Mass Spectrometry (ICP-MS) at the National Research Center for Geoanalysis, Beijing. A certified reference material JDo-1 (dolostone) was measured after every nine samples and the analytical uncertainties monitored by JDo-1 were <3% for Mg and <2% for Ca. For iodine analysis, 1 mL supernatant was used, and 3% tertiary amine solution was added to the supernatant, and then diluted to 0.5% with MQ water to stabilize iodine (Lu et al. 2010; Hardisty et al. 2017). The iodine content was measured within 48 hours to avoid any iodine loss (Lu et al. 2010), using a MC-ICP-MS (Neptune Plus, Thermo Fisher Scientific, Germany) at the National Research Center of Geoanalysis, Beijing. The sensitivity of iodine was tuned to ~1,500 kcps for a 1 ppb standard in the MC-ICP-MS. The rinse solution used for each individual analyses contains 0.5% HNO_3, 0.5% tertiary amine, and 50 μg/g Ca, and the typical rinse time is ~1 min. Analytical uncertainties for ^{127}I monitored by the standard GSR 12 and duplicate samples are $\leq 6\%$ (1σ), and the long term accuracy is checked by repeated analyses of the reference material GSR 12 (Shang et al. 2019). The detection limit of I/(Ca+Mg) is on the order of 0.1 μmol/mol.

For major element analyses of green and red shales, about 50 mg sample powder was dissolved in 250 mg lithium metaborate at 990 °C for 20 min and then diluted to 100 ml by MQ before element measurement using Inductively Coupled Plasma Optical Emission Spectrometry (ICP-OES) at China University of Geosciences (Beijing). Fe(II)/Fe(III) ratio of samples was determined by ICP-OES and titration technique. The accuracy of all ICP-OES analyses is better than 5% (relative) for analyzed elements. For REE+Y analysis of the ankerite, ~100 mg of fine powder for each sample was weighed out and then rinsed with MQ water four times to remove clay minerals. In order to further minimize the potential influence of terrigenous components on REE+Y, carbonate samples were dissolved using 5% acetic acid rather than other strong acids. Following the method described in Zhang et al. (2015b), the pre-leached 30% of total carbonate has been removed, only the following dissolved 40% of total carbonate was separated for REE analysis, and the last 30% of total carbonate remained undissolved in order to avoid contamination from non-carbonate minerals. The trace elements were measured in a PerkinElmer NexION 300Q Inductively Coupled Plasma Mass Spectrometry (ICP-MS) at National Research Center for Geoanalysis, Beijing. The accuracy of all ICP-MS analyses is better than 5−10% (relative) for analyzed elements.

For carbon isotope analysis, sample powders were drilled from polished slabs, avoiding weathered surfaces and recrystallized areas. All the analyses were conducted at the State Key Laboratory of Biogeology and Environmental Geology, China University of Geosciences (Wuhan). About 150–400 μg of powder was placed in a 10 mL Na-glass vial, sealed with a butyl rubber septum, and reacted with 100% phosphoric acid at 72 °C after flushing with helium. The evolved CO_2 gas was analyzed for $\delta^{13}C$ and $\delta^{18}O$ using a MAT 253 mass-spectrometer coupled directly to a Finnigan Gasbench II interface (Thermo Scientific). Isotopic values are reported as per mille relative to the Vienna Pee Dee belemnite (VPDB) standard. Analytical precision was better than ±0.1‰ for $\delta^{13}C$ and $\delta^{18}O$ based on replicate analyses of two laboratory standards (GBW 04416 and GBW 04417). The $\delta^{13}C$ and $\delta^{18}O$ of these two laboratory standards are 1.61‰ and −11.59‰, and −6.06‰ and −24.12‰, respectively.

RESULTS

The MRBs of the Xiamaling Formation are characterized by laterally continuous, red shale layers alternating with green shales at centimeter to decimeter scales (Fig. 3a). Within a single red bed, the color is typically uniform (Fig. 3b). The red beds contain similar Fe(II) but elevated Fe(III) contents relative to adjacent green beds (Table 1). Petrographic and X-ray diffraction analyses indicate that both the red and green shales are mainly composed of illite and quartz, but the red beds have significantly higher hematite content ($TFe_2O_3 = 8.09\pm1.30$ wt%, $n = 9$) than that of green beds ($TFe_2O_3 = 5.00\pm0.38$ wt%, $n = 7$; Table 1; Fig. 3c).

The MRBs are compositionally homogenous (Fig. 3d), with abundant flakes of sub-micron-sized hematite disseminated throughout the illite matrix (Fig. 3e–m), as confirmed by EBSD analyses (Fig. 3n) and consistent with the results of X-ray diffraction. Quantitative EDS analyses of larger flake aggregates (>2 μm) show that they are composed of Fe and O, with a molar ratio of 2:3, indicative of hematite (Fig. 3o). Further element mapping also indicates that they consist mainly of Fe and O, occasionally with minor amounts of Ti (Fig. 4).

Backscattered electron imaging shows that the sub-micron-sized hematite particles are flaky in shape and vary widely in size, from <50 nm to 1000 nm (Fig. 3e–m). Rigid, detrital quartz grains provide pressure shadows where the weakly compacted, flaky hematite nanoparticles are randomly oriented and dispersed in illite matrix instead of being concentrated in residual pore space (Fig. 3e–j). The hematite grains are euhedral to subhedral in morphology (Fig. 3k). Larger spherical aggregates (1–20 μm in diameter) composed of hematite particles are also dispersed in the pressure shadow zones (Fig. 3g–j). These aggregates comprise hematite particles that display face-to-face and face-to-edge ("cardhouse") contacts. These hematite flakes are also present in shortly transported mud intraclasts, and bend around rigid detrital grains (Fig. 3l and m).

Ankerite concretions are wrapped by shale laminae (Fig. 5a). They are composed of euhedral to subhedral ankerite grains with some illite and quartz matrix (Fig. 5b and c). The ankerite grains are composed of Ca, Mg, Fe, Mn, C and O, and their Fe and Mn contents are 8.14±0.41 wt% and 1.15±0.17 wt% (n = 122), respectively (Fig. 5d–o; Table S1). The carbon isotope composition ($\delta^{13}C$) of ankerite concretions is −6.9±0.9‰ (n = 9; Fig. 5p; Table 2), lower than that of contemporaneous seawater (~0‰; Guo et al. 2013). The ankerite concretions within the MRBs have I/(Ca+Mg) values between 0.08 and 0.23 μmol/mol (0.16±0.05) (Fig. 5q; Table 2). Post Archean Australian Shale-normalized REE+Y patterns of ankerite concretions show a depletion of light REEs (Pr_{SN}/Yb_{SN} = 0.41±0.09), moderate enrichment of middle REEs, slightly positive Eu anomalies (Eu/Eu* = 1.10±0.09), positive Ce anomalies (Ce/Ce* = 1.32±0.04), and low Y/Ho ratios (24.39±2.26) (Fig. 5r; Table 3).

DISCUSSION

The genesis of MRBs is poorly understood. The diagenetic oxidation of Fe(II)-bearing marine sediments has been proposed to explain some Phanerozoic MRBs (e.g., Hu et al. 2012), which was supported by the observation of epitaxial growth of hexagonal hematite (Eren and Kadir 1999). However, this phenomenon has not been observed in this study (Fig. 3). In addition, hematite did not occur as grain coating, likely refuting the precipitation of iron-hydroxides though the mixing of upwardly diffused Fe(II) from deeper anoxic porewater with hypoxic porewater in upper sediment pile. Other researchers have proposed that detrital iron oxides supplied to marine sediments could have created MRBs (e.g., Franke and Paul 1980). However, the euhedral to subhedral morphology of hematite nanoparticles (Fig. 3k) in the Xiamaling MRBs suggests that the particles were initially precipitated as oxyhydroxides in the water column, rather than distally transported from a continental source. Thus, continental or distally derived iron oxide particles are unlikely the dominant source for the hematite particles in the Xiamaling MRBs. The lack of evidence for potential precursor ferrous Fe minerals such as greenalite (e.g., Rasmussen et al. 2016) or green rust (e.g., Halevy et al. 2017), suggests that the hematite is unlikely to be derived from post-depositional oxidation of reduced Fe phases. In addition, the hematite flakes bend around rigid gains (Fig. 3l and m), indicating that Fe-hydroxides were formed before obvious compaction of sediments. The hematite aggregates (Fig. 3e–j) resemble partial floccules in clay slurries of freshly deposited, modern marine muds (Nishida et al. 2013; Deirieh et al. 2018), which suggests that the precursor of hematite nanoparticles were more likely settled down from the water column as loosely bounded iron oxyhydroxide flocs in water-rich mud.

Iron oxyhydroxide precipitation from the water column requires a dissolved Fe(II) source. Precambrian oceans are considered to have been dominantly ferruginous (e.g., Poulton and Canfield 2011) with a Fe(II) reservoir largely sourced from hydrothermal venting (e.g., Rasmussen et al. 2012; Bekker et al. 2014) and the reduction of continentally-sourced Fe(III)-bearing sediments (e.g., Li et al. 2015). Europium anomalies in marine chemical sediments have been used to track hydrothermal input into seawater, given that high temperature hydrothermal brines are typically enriched in Eu (e.g., Derry and Jacobsen 1990). The preservation of slight positive Eu anomalies in the ankerite concretions (Eu/Eu* = 1.10±0.09) may suggests a distal hydrothermal influence on the chemistry of the Xiamaling basin. There is evidence from the underlying stratified siderite ($FeCO_3$) deposits for active dissimilatory iron reduction prior to MRB deposition [dissimilatory iron reduction: $4Fe(OH)_3 + CH_2O \rightarrow FeCO_3 + 3Fe_{aq}^{2+} + 6OH^{-} + 4H_2O$; Canfield et al. 2018; Tang et al. 2018]. This dissimilatory iron reduction would have led to the release of Fe_{aq}^{2+} into the water column if the bottom seawater was anoxic or through ‘iron shuttle’ in hypoxic conditions (Lyons and Severmann 2006). Therefore, we suggest that the Fe(II) reservoir of the Xiamaling basin was accumulated from a combination of distal hydrothermal and continental sources, as it has been suggested for the Paleoproterozoic oceans (Fig. 6; Li et al. 2015). Considering the general lack of significant positive Eu anomalies (Table 3), we argue that recycled continentally-sourced iron through dissimilatory iron reduction may have been the major iron source for the Xiamaling MRBs with possible influence from distal hydrothermal fluids (Fig. 6).

Some studies on Cr isotopes in marine ironstones and shales suggested that the atmospheric oxygen level of mid-Proterozoic was <0.1–1% PAL (Planavsky et al. 2014; Cole et al. 2016). However, in North China, the lack of V-enrichment in the black shales from the ~1.40–1.35 Ga Xiamaling Formation (upper Member II) and a carbon-oxygen cycle model indicate that the atmospheric oxygen levels were >4% PAL (Zhang et al. 2016). In North Australia, the enrichment of redox-sensitive metals in the black shales from the upper Velkerri Formation suggests an episode of increased ocean oxygenation at ~1.4 Ga (Cox et al. 2016; Mukherjee and Large 2016). In West Siberia, Fe speciation, redox-sensitive metal concentrations and the occurrence of eukaryotic microfossils from the basinal sedimentary rocks in the Kaltasy Formation (Arlan Member) indicate the existence of weakly oxygenated deep marine waters at ~1.4 Ga (Sperling et al. 2014). In this study, ankerite concretions are wrapped by shale laminae, indicative of an early diagenetic origin (cf. Liu et al. 2019b). The relatively high Fe and Mn contents and negative carbon isotopes of ankerite grains in the concretions (Fig. 5f and p; Tables 2 and S1), likely indicate that the concretions were formed in an environment from hypoxic Mn reduction to anoxic Fe reduction zone in sediments (cf. Tang et al. 2018; Liu et al. 2019b, 2020). Although the chemistry of porewater is distinct from that of the overlying bottom seawater, it should be strongly influenced by and therefore could indirectly reflect the chemistry of overlying seawater (e.g., Liu et al. 2019b, 2020). The positive Ce anomalies (Ce/Ce* >1.3) and low Y/Ho ratios (<27) of early diagenetic ankerite concretions within the MRBs suggest the presence of active Mn cycling in porewater and potentially in the water column. Cerium can be effectively removed from oxic seawater due to scavenging by precipitating Mn oxides, which can lead to positive Ce anomalies in Mn oxides (e.g., Bau et al. 1997; Planavsky et al. 2010). On the other hand, Yttrium is comparatively stable in seawater relative to the other REEs that are scavenged by precipitating Fe-Mn (oxyhydr)oxides. This can lead to low Y/Ho ratios in Mn oxide-bearing sediments (Bau et al. 1997). However, Mn oxides readily undergo reductive dissolution under anoxic conditions and are rarely preserved in the sedimentary record (Johnson et al. 2016). We suggest that abundant Mn (oxyhydr)oxides may have been precipitated from water column and their reductive dissolution during early diagenesis may have led to porewaters enriched in Ce and depleted in Y relative to ambient seawater, which is captured by contemporaneous ankerite precipitation (cf. Tang et al. 2018; Liu et al. 2019b, 2020). Due to the high redox potential of Mn(IV)/Mn(II) (+1.23 V; Lide 2004), only O_2 or hyperoxides can efficiently oxidize Mn^{2+} in natural environments (Johnson et al. 2016; Ossa et al. 2018). Thus, the preservation of Mn oxides on the seafloor requires the presence of sufficient O_2 (Tostevin et al. 2016) in the overlying seawater in order to produce abundant Mn oxyhydroxides and prevent their complete reduction and dissolution during settling. We suggest that the high Mn contents and REE+Y data in the ankerite concretions are probably indicative of active redox cycle of Mn and hypoxic water column.

No relics of carbonate mud, which precipitated from oxygen-bearing water column, were identified in the ankerite concretions (Fig. 5). Therefore, the non-zero I/(Ca+Mg) values in the early diagenetic ankerite concretions (Fig. 5q; Table 2) may indicate that iodate (IO_3^-) was retained in the porewater during early diagenesis (e.g., Mn reduction stage; cf. Lu et al. 2010) rather than sourced from water-column-precipitated carbonate muds. Under reducing conditions iodate is reduced to iodide (I^-) which is incompatible in carbonates, and therefore non-zero I/(Ca+Mg) values suggest oxidizing conditions during carbonate formation (Lu et al. 2010). Although iodine loss is expected during diagenesis, late-stage diagenesis is unlikely to increase the iodine contents of carbonates (Hardisty et al. 2017). The non-zero I/(Ca+Mg) values in early diagenetic ankerite concretions may be explained by the presence of trace amount of O_2 in early diagenetic porewater. The oxygen concentration of bottom seawater is commonly higher than that of porewater, since molecular diffusion of oxygen and aerobic degradation of organic matter would dramatically decrease the oxygen concentration (e.g., Glud 2008; Zhang et al. 2017). The retaining of molecular oxygen in porewater is possibly indicative of a hypoxic bottom waters. Owing to the increase of shallow seawater $[O_2]$ by primary productivity, and the decrease of bottom seawater $[O_2]$ by aerobic degradation of organic matter and invasion of deep ferruginous seawater, the shallow seawater should have higher oxygen concentration than that of bottom seawater (e.g., Wang et al. 2020).

There are several mechanisms by which Fe(II) can be oxidized in the water column. In oxygenated seawater, abiotic oxidation of Fe(II) by free O_2 may dominate. Under anoxic conditions, iron oxyhydroxide may be produced biologically during anoxygenic photosynthesis (e.g., Kappler et al. 2005). In hypoxic seawater, Fe(II) oxidation is facilitated by microaerophilic chemosynthesizers (e.g., Chan et al. 2016; Lin et al. 2019). The activity of microaerobic Fe(II)-oxidizing bacteria near the water–sediment interface has been suggested as the major cause for iron oxide enrichment in Phanerozoic red beds, based on fossil evidence of Fe(II)-oxidizing bacteria (Mamet and Préat 2006). Considering the hypoxic water column condition, we argue that the iron oxyhydroxides in the Xiamaling MRBs were likely formed by the oxidation of Fe(II) in water column though abiotic and microbially-mediated processes, although the fossil record of microaerophilic Fe(II)-oxidizing bacteria were not observed.

IMPLICATIONS

Some MRBs are interpreted formed during early diagenesis under highly oxic, oligotrophic, and probably low-productivity seawater conditions (e.g., Hu et al. 2006). In this study, however, evidence supports the primary origin of the Xiamaling MRBs. More MRBs are interpreted as having formed in stratified water columns with iron oxyhydroxide precipitation near the Fe-redox boundary during the termination of ocean anoxic events (e.g., Neuhuber et al. 2007; Wang et al. 2011; Hu et al. 2012; Song et al. 2017; Liu et al. 2019b, 2020). In such an interpretation, the bottom water and porewater should have been ferruginous. The non-zero I/(Ca+Mg) ratios revealed from the Xiamaling MRBs, however, indicate the presence of minor amount free O_2 in porewater. In addition, residence time of Fe(II) in oxygenated seawater is short; however, the accumulation of thick MRBs (~12 m) requires a sustained (~1.8 myr, cf. Zhang et al. 2015a) Fe(II) supply from ferruginous water columns. These seemly contradictory data can be reconciled by the presence of sustained deep ferruginous seawaters, in which Fe(II) accumulated from distal hydrothermal fluids and diffused porewater from sediments with active dissimilatory iron reduction (Fig. 6). Marine transgression would bring ferruginous deep bottom seawater into moderately oxygenated shallower seawater. If hematite in Phanerozoic MRBs is of similar origin, the development of MRBs in stratigraphic succession may indicate the transformation from anoxic to moderately oxygenated conditions in seawaters with the existence of adjacent ferruginous water mass rather than immediately to highly oxygenated conditions. The occurrence of Xiamaling red beds, therefore, supports the viewpoint that the oxygen level of surface ocean and atmosphere at ~1.4 Ga was more dynamic than previously thought (e.g. Planavsky et al. 2018).

The chamosite and siderite-rich iron formations in the lower Member II of the Xiamaling Formation have been interpreted as forming in highly Fe(II)-enriched ferruginous seawater above storm wave base (Tang et al. 2017, 2018; Canfield et al. 2018). The transition from siderite-rich sediments to MRBs in the Xiamaling Formation may indicate a prominent decrease in seawater Fe(II) concentrations (cf. Song et al. 2017) and a slight increase in seawater oxygenation (Zhang et al. 2016; Wang et al. 2017). A diminishing hydrothermal

Fe(II) input into the depositional basin is supported by a decrease in Eu anomalies in the Xiamaling Formation sediments (Tang et al. 2018). The slight oxygenation in bottom seawaters also find supports from the geochemical evidence of increasing iodine concentrations and aerobic Mn cycling recorded in the ankerite concretions from the Xiamaling Formation.

ACKNOWLEDGMENTS

The study was supported by the National Natural Science Foundation of China (Nos. 41930320, 41972028), the Key Research Program of the Institute of Geology & Geophysics, CAS (No. IGGCAS-201905), and by the Fundamental Research Funds for the Central Universities (No. 2652018005). Maxwell Lechte acknowledges funding from the Fonds de Recherche du Québec—Nature et Technologies. We appreciate the constructive comments and suggestions from the editor and two anonymous reviewers, which improved the paper greatly. Thanks are also given to Ganqing Jiang for his critical comments, and to Mohan Shang, Yang Li, Haoming Wei and Zhipeng Wang for their assistance in fieldwork.

REFERENCES CITED

Anbar, A.D., and Knoll, A.H. (2002) Proterozoic ocean chemistry and evolution: a bioinorganic bridge?. Science, 297, 1137–1142.

Bau, M., Möller, P., and Dulski, P. (1997) Yttrium and lanthanides in eastern Mediterranean seawater and their fractionation during redox-cycling. Marine Chemistry, 56, 123–131.

Bekker, A., Planavsky, N.J, Krapež, B., Rasmussen, B., Hofmann, A., Slack, J.F., Rouxel, O.J., and Konhauser, K.O. (2014). Iron Formations: Their Origins and Implications for Ancient Seawater Chemistry. In H. Holland and K. Turekian, Eds., Treatise on Geochemistry, 9, p. 561–628. Elsevier, Amsterdam.

Canfield, D.E., Zhang, S., Wang, H., Wang, X., Zhao, W., Su, J., Bjerrum, C.J., Haxen, E.R., and Hammarlund, E.U. (2018) A Mesoproterozoic iron formation. Proceedings of the National Academy of Sciences, 115, E3895–E3904.

Chan, C.S., Emerson, D., and Luther III, G.W. (2016) The role of microaerophilic Fe-oxidizing micro-organisms in producing banded iron formations. Geobiology, 14, 509–528.

Cox, G.M., Jarrett, A., Edwards, D., Crockford, P.W., Halverson, G.P., Collins, A.S., Poirier, A., and Li, Z.X. (2016) Basin redox and primary productivity within the Mesoproterozoic Roper Seaway. Chemical Geology, 440, 101–114.

Deirieh, A., Chang, I.Y., Whittaker, M.L., Weigand, S., Keane, D., Rix, J., Germaine, J.T., Joester, D., and Flemings, P.B. (2018) Particle arrangements in clay slurries: The case against the honeycomb structure. Applied Clay Science, 152, 166–172.

Derry, L.A., and Jacobsen, S.B. (1990) The chemical evolution of Precambrian seawater: evidence from REEs in banded iron formations. Geochimica et Cosmochimica Acta, 54, 2965–2977.

Eren, M., and Kadir, S. (1999) Colour origin of upper Cretaceous pelagic red sediments within the Eastern Pontides, northeast Turkey. International Journal of Earth Sciences, 88, 593–595.

Franke, W., and Paul, J. (1980) Pelagic redbeds in the Devonian of Germany—deposition and diagenesis. Sedimentary Geology, 25, 231–256.

Galloway, J.J. (1922) Red limestones and their geologic significance (Abstract with discussion by I.C. White, G.H. Chadwick, T.W. Stanton, and R.S. Bassler). Geological Society of America Bulletin, 33, 105–107.

Glud, R.N. (2008) Oxygen dynamics of marine sediments. Marine Biology Research, 4, 243–289.

Guo, H., Du, Y., Kah, L.C., Huang, J., Hu, C., Huang, H., and Yu, W. (2013) Isotopic composition of organic and inorganic carbon from the Mesoproterozoic Jixian Group, North China. Implications for biological and oceanic evolution. Precambrian Research, 224, 169–183.

Halevy, I., Alesker, M., Schuster, E.M., Popovitz-Biro, R. and Feldman, Y. (2017) A key role for green rust in the Precambrian oceans and the genesis of iron formations. Nature Geoscience, 10, 135–139.

Hardisty, D.S., Lu, Z., Bekker, A., Diamond, C.W., Gill, B.C., Jiang, G., Kah, L.C., Knoll, A.H., Loyd, S.J., Osburn, M.R., Planavsky, N.J., Wang, C.J., Zhou, X.L., and Lyons, T.W. (2017) Perspectives on Proterozoic surface ocean redox from iodine contents in ancient and recent carbonate. Earth and Planetary Science Letters, 463, 159–170.

Hu, X.M., Wang, C.S., Li, X.H., and Jansa, L. (2006) Upper Cretaceous oceanic red beds in southern Tibet: Lithofacies, environments and colour origin. Science in China Series D: Earth Sciences, 49, 785–795.

Hu, X.M., Scott, R.W., Cai, Y.F., Wang, C.S., and Melinte-Dobrinescu, M.C. (2012) Cretaceous oceanic red beds (CORBs): Different time scales and models of origin. Earth-Science Reviews, 115, 217–248.

Johnson, K.S., Gordon, R.M., and Coale, K.H. (1997) What controls dissolved iron concentrations in the world ocean?. Marine chemistry, 57, 137–161.

Johnson, J.E., Webb, S.M., Ma, C., and Fischer, W.W. (2016) Manganese mineralogy and diagenesis in the sedimentary rock record. Geochimica et Cosmochimica Acta, 173, 210–231.

Kappler, A., Pasquero, C., Konhauser, K.O., and Newman, D.K. (2005) Deposition of banded iron formations by anoxygenic phototrophic Fe(II)-oxidizing bacteria. Geology, 33, 865–868.

Li, W., Beard, B.L., and Johnson, C.M. (2015) Biologically recycled continental iron is a major component in banded iron formations. Proceedings of the National Academy of Sciences, 112, 8193–8198.

Lide, D.R. Ed. (2004) CRC handbook of chemistry and physics, 2661p. CRC Press, Boca Raton, FL.

Lin, Y.T., Tang, D.J., Shi, X.Y., Zhou, X.Q., and Huang, K.J. (2019) Shallow-marine ironstones formed by microaerophilic iron-oxidizing bacteria in terminal Paleoproterozoic. Gondwana Research, 76, 1–18.

Liu, M., Chen, D.Z., Zhou, X.Q., Tang, D.J., Them II, T. R., Jiang, M.S. (2019a) Upper Ordovician marine red limestones, Tarim Basin, NW China: A product of an oxygenated deep ocean and changing climate?. Global and Planetary Change, 183, 103032.

Liu, A.Q., Tang, D.J., Shi, X.Y., Zhou, L.M., Zhou, X.Q., Shang, M.H., Li, Y., and Song, H.Y. (2019b) Growth mechanisms and environmental implications of carbonate concretions from the ~1.4 Ga Xiamaling Formation, North China. Journal of Palaeogeography, 8, 20.

Liu, A.Q., Tang, D.J., Shi, X.Y., Zhou, X.Q., Zhou, L.M., Shang, M.H., Li, Y., and Fang, H. (2020) Mesoproterozoic oxygenated deep seawater recorded by early diagenetic carbonate concretions from the Member IV of the Xiamaling Formation, North China. Precambrian Research, in press, https://doi.org/10.1016/j.precamres.2020.105667.

Lu, Z.L., Jenkyns, H.C., and Rickaby, R.E. (2010) Iodine to calcium ratios in marine carbonate as a paleo-redox proxy during oceanic anoxic events. Geology, 38, 1107–1110.

Luo, G.M., Hallmann, C., Xie, S., Ruan, X., and Summons, R.E. (2015) Comparative microbial diversity and redox environments of black shale and stromatolite facies in the Mesoproterozoic Xiamaling Formation. Geochimica et Cosmochimica Acta, 151, 150–167.

Lyons, T.W., and Severmann, S. (2006) A critical look at iron paleoredox proxies: New insights from modern euxinic marine basins. Geochimica et Cosmochimica Acta, 70, 5698–5722.

Lyons, T.W., Reinhard, C.T., and Planavsky, N.J. (2014) The rise of oxygen in Earth's early ocean and atmosphere. Nature, 506, 307–315.

Ma, L.F., Qiao, X.F., Ming, L.R., Fan, B.X., and Ding, X.Z. (2002) Atlas of Geological Maps of China, 348 p. Geological Press, Beijing (in Chinese).

Mamet, B., and Préat, A. (2006) Iron-bacterial mediation in Phanerozoic red limestones: state of the art. Sedimentary Geology, 185, 147–157.

Mukherjee, I., and Large, R.R. (2016) Pyrite trace element chemistry of the Velkerri Formation, Roper Group, McArthur Basin: Evidence for atmospheric oxygenation during the Boring Billion. Precambrian Research, 281, 13–26.

Neuhuber, S., Wagreich, M., Wendler, I., and Spötl, C. (2007) Turonian oceanic red beds in the Eastern Alps: Concepts for palaeoceanographic changes in the Mediterranean Tethys. Palaeogeography, Palaeoclimatology, Palaeoecology, 251, 222–238.

Nishida, N., Ito, M., Inoue, A., and Takizawa, S. (2013) Clay fabric of fluid-mud deposits from laboratory and field observations: Potential application to the stratigraphic record. Marine Geology, 337, 1–8.

Ossa, F.O., Hofmann, A., Wille, M., Spangenberg, J.E., Bekker, A., Poulton, S.W., Eickmann, B., and Schoenberg, R. (2018) Aerobic iron and manganese cycling in a redox-stratified Mesoarchean epicontinental sea. Earth and Planetary Science Letters, 500, 28–40.

Planavsky, N., Bekker, A., Rouxel, O.J., Kamber, B., Hofmann, A., Knudsen, A., and Lyons, T.W. (2010) Rare earth element and yttrium compositions of Archean and Paleoproterozoic Fe formations revisited: new perspectives on the significance and mechanisms of deposition. Geochimica et Cosmochimica Acta, 74, 6387–6405.

Planavsky, N. J., McGoldrick, P., Scott, C.T., Li, C., Reinhard, C.T., Kelly, A.E., Chu, X., Bekker, A., Love, G.D., and Lyons, T.W. (2011) Widespread iron-rich conditions in the mid-Proterozoic ocean. Nature, 477, 448–451.

Planavsky, N.J., Reinhard, C.T., Wang, X., Thomson, D., McGoldrick, P., Rainbird, R. H., Johnson, T., Fischer, W.W., and Lyons, T.W. (2014) Low Mid-Proterozoic atmospheric oxygen levels and the delayed rise of animals. Science, 346, 635–638.

Planavsky, N.J., Cole, D.B., Isson, T.T., Reinhard, C.T., Crockford, P.W., Sheldon, N.D., and Lyons, T.W. (2018) A case for low atmospheric oxygen levels during Earth's middle history. Emerging Topics in Life Sciences, 2, 149–159.

Poulton, S.W., and Canfield, D.E. (2011) Ferruginous conditions: a dominant feature of the ocean through Earth's history. Elements, 7, 107–112.

Poulton, S.W., Fralick, P.W., and Canfield, D.E. (2010) Spatial variability in oceanic redox structure 1.8 billion years ago. Nature Geoscience, 3, 486–490.

Préat, A.R., de Jong, J.T., Mamet, B.L., and Mattielli, N. (2008) Stable iron isotopes and microbial mediation in red pigmentation of the Rosso Ammonitico (Mid-Late Jurassic, Verona area, Italy). Astrobiology, 8, 841–857.

Rasmussen, B., Fletcher, I.R., Bekker, A., Muhling, J.R., Gregory, C.J. and Thorne, A.M. (2012) Deposition of 1.88-billion-year-old iron formations as a consequence of rapid crustal growth. Nature, 484, 498–501.

Rasmussen, B., Muhling, J.R., Suvorova, A., and Krapež, B. (2016) Dust to dust: Evidence for the formation of “primary” hematite dust in banded iron formations via oxidation of iron silicate nanoparticles. Precambrian Research, 284, 49–63.

Rasmussen, B., Muhling, J.R., and Fischer, W.W. (2019) Evidence from laminated chert in banded iron formations for deposition by gravitational settling of iron-silicate muds. Geology, 47, 167–170.

Ryan, P.C., and Reynolds, R.C. (1996) The origin and diagenesis of grain-coating serpentinechlorite in Tuscaloosa Formation sandstone, US Gulf Coast. American Mineralogist, 81, 213–225.

Shang, M.H., Tang, D.J., Shi, X.Y., Zhou, L.M., Zhou, X.Q., Song, H.Y., and Jiang, G.Q. (2019) A pulse of oxygen increase in the early Mesoproterozoic ocean at *ca.* 1.57–1.56 Ga. Earth and Planetary Science Letters, 527, 115797.

Song, H.J., Jiang, G.Q., Poulton, S.W., Wignall, P.B., Tong, J.N., Song, H.Y., An, Z.H., Chu, D.L., Tian, L., She, Z.B., and Wang, C.S. (2017) The onset of widespread marine red beds and the evolution of ferruginous oceans. Nature communications, 8, 399.

Sperling, E.A., Rooney, A.D., Hays, L., Sergeev, V.N., Vorob'eva, N.G., Sergeeva, N.D., Selby, D., Johnston, D.T. and Knoll, A.H. (2014) Redox heterogeneity of subsurface waters in the Mesoproterozoic ocean. Geobiology, 12, 373–386.

Tang, D.J., Shi, X.Y., Jiang, G.Q., Zhou, X.Q., and Shi, Q. (2017) Ferruginous seawater facilitates the transformation of glauconite to chamosite: An example from the Mesoproterozoic Xiamaling Formation of North China. American Mineralogist, 102, 2317–2332.

Tang, D.J., Shi, X.Y., Jiang, G.Q., Wu, T., Ma, J.B., and Zhou, X.Q. (2018) Stratiform siderites from the Mesoproterozoic Xiamaling Formation in North China: Genesis and environmental implications. Gondwana Research, 58, 1–15.

Tostevin, R., Wood, R., Shields, G., Poulton, S., Guilbaud, R., Bowyer, F., Penny, A., He, T., Curtis, A., and Hoffmann, K. (2016) Low-oxygen waters limited habitable space for early animals. Nature Communications, 7, 12818.

Van Houten, F.B. (1973) Origin of red beds: a review—1961–1972. Annual Review of Earth and Planetary Sciences, 1, 39–61.

Wang, H.Z., Chu, X.C., Liu, B.P., Hou, H.F., and Ma, L.F. (1985) Atlas of the Palaeogeography of China. 143 p, Cartographic Publishing House, Beijing (in Chinese and English).

Wang, C.S., Hu, X.M., Huang, Y.J., Wagreich, M., Scott, R., and Hay, W. (2011) Cretaceous oceanic red beds as possible consequence of oceanic anoxic events. Sedimentary Geology, 235, 27–37.

Wang, X.M., Zhang, S.C., Wang, H.J., Bjerrum, C.J., Hammarlund, E.U., Haxen, E.R., Su, J., Wang, Y., and Canfield, D.E. (2017) Oxygen, climate and the chemical evolution of a 1400 million year old tropical marine setting. American Journal of Science, 317, 861–900.

Wang, H.Y., Zhang Z.H., Li, C., Algeo, T.J., Cheng, M., and Wang, W. (2020) Spatiotemporal redox heterogeneity and transient marine shelf oxygenation in the Mesoproterozoic ocean. Geochimica et Cosmochimica Acta, 270, 201–217.

Zhang, S.H., Zhao, Y., Yang, Z.Y., He, Z.F., and Wu, H. (2009) The 1.35 Ga diabase sills from the Northern North China Craton: implications for breakup of the Columbia (Nuna) supercontinent. Earth and Planetary Science Letters, 288, 588–600.

Zhang, S.C., Wang, X.M., Hammarlund, E.U., Wang, H.J., Costa, M.M., Bjerrum, C.J., Connelly, J.N., Zhang, B.M., Bian, L.Z., and Canfield, D.E. (2015a) Orbital forcing of climate 1.4 billion years ago. Proceedings of the National Academy of Sciences, 112, E1406–E1413.

Zhang, K., Zhu, X.K., and Yan, B. (2015b) A refined dissolution method for rare earth element studies of bulk carbonate rocks. Chemical Geology, 412, 82–91.

Zhang, S.C., Wang, X.M., Wang, H.J., Bjerrum, C.J., Hammarlund, E.U., Costa, M.M., Connelly, J.N., Zhang, B.M., Su, J., and Canfield, D.E. (2016) Sufficient oxygen for animal respiration 1,400 million years ago. Proceedings of the National Academy of Sciences, 113, 1731–1736.

Zhang, S.C., Wang, X.M., Wang, H., Hammarlund, E.U., Su, J., Wang, Y., and Canfield, D.E.

(2017) The oxic degradation of sedimentary organic matter 1400 Ma constrains atmospheric oxygen levels. Biogeosciences Discussions, 14, 2133–2149.

Zou, Y., Liu, D.N., Zhao, F.H., Kuang, H.W., Song, C.G., Sun, Y.X., Zhou, R., and Cheng, J.B. (2019) Reconstruction of nearshore chemical conditions in the Mesoproterozoic: evidence from red and grey beds of the Yangzhuang formation, North China Craton. International Geology Review, in press, https://doi.org/10.1080/00206814.2019.1647469

Figure Captions

Figure 1. (**a**) Simplified paleogeographic map of North China during Mesoproterozoic, showing location of the studied area (modified after Wang et al. 1985). (**b**) Simplified geological map of the studied sections (modified after Ma et al. 2002) (**c**) Generalized stratigraphic column of the Xiamaling Formation in North China, showing the studied marine red bed interval and the underling iron formation interval.

Figure 2. Photographs showing major depositional facies in Member II of the Xiamaling Formation. (**a**) Gray to green fine-grained sandstone and siltstone in the lower unit of the Member II. (**b**) Green fine-grained sandstone in the lower unit of Member II. (**c**) Gray siltstone in the lower unit of the Member II. (**d**) Siderite layers interbedded with green siltstone in the lower unit of Member II. (**e**) Alternating red and green shale beds, with light colored ankerite concretions in the middle unit of Member II. (**f**) Light colored ankerite concretions and green shale. (**g**) Ankerite concretions in alternating red and green shale beds. (**h**) Alternation of green and gray shale beds in the upper unit of Member II.

Figure 3. Petrographic and geochemical analysis results of MRBs from the Xiamaling Formation, North China. (**a**) Field photographs showing alternating red and green shale beds.

(**b**) Close view showing the alternation of red and green shale beds. (**c**) X-ray diffraction results, showing that red beds are mainly composed of illite, quartz and hematite, while the neighboring green beds are dominated by illite and quartz, without hematite. (**d**) Photomicrograph showing red beds with relatively homogeneous color. (**e**) BSE image showing abundant hematite particles (light gray) in illite matrix (medium gray) surrounded by detrital quartz grains (dark gray). (**f**) BSE image of red beds, showing randomly orientated nanoparticles that form aggregates (ag) with multiple face-to-face (F-F) flakes and flakes with face-to-edge (F-E) contacts. (**g–j**) BSE images showing randomly oriented hematite nanoparticles and 1–20 μm larger clump of hematites. (**k**) BSE image with high magnification, showing hexagonal morphology of a hematite polyhedron. (**l**) BSE image showing an intraclast with hematite particles parallel to bedding. (**m**) BSE image with high magnification, showing plastic deformation of the intraclast around a rigid detrital grain. (**n**) Electron back-scattered diffraction analysis result of flaky hematite particles. (**o**) Quantitative EDS analysis result of a hematite aggregate, showing its composition of Fe and O, with Fe/O molar ratio of 2:3.

Figure 4. Element mapping and point analysis results, showing hematite aggregate mainly composed of Fe and O, with minor amount of Ti.

Figure 5. Petrographic and geochemical analysis results of ankerite concretions from the Xiamaling Formation, North China. (**a**) Ankerite concretion wrapped by red/green shale laminae (dashed lines). (**b**) Photomicrograph showing that ankerite concretions were mainly composed of euhedral to subhedral ankerite grains with some siliciclastic matrix. (**c**) X-ray diffraction results, showing that ankerite concretions are composed of ankerite, illite and quartz. (**d**) BSE image of ankerite concretion. (**e**) EDS spectrum of an ankerite grain. (**f**)

Cross plot of Mn vs. Fe, showing the relatively high Fe and Mn contents of ankerite grains. (**g**)-(**o**) EDS element mapping result of boxed area in panel **d**. (**p**) Cross plot of C isotope vs. O isotope, showing depleted carbon isotope composition of ankerite concretions. (**q**) I/(Ca+Mg) analysis result of early diagenetic ankerite concretions occurring in the red and green shale beds. (**r**) REE+Y patterns of acetic acid (5%) leached ankerite concretions, showing the positive Ce anomalies and low Y/Ho ratios.

Figure 6. A proposed depositional model for the Xiamaling iron formations (**a**) and MRBs (**b**). The MRBs were formed in the moderately oxygenated seawater with deeper ferruginous seawater. The iron in seawater was sourced from distal hydrothermal fluids and continental sediments by dissimilatory iron reduction (cf. Lyons and Severmann 2006; Li et al. 2015). The alternation of red and green beds was probably regulated by the amount of deposited organic matter (Wang et al. 2017). The thick accumulation of MRBs probably required a long-lasting adjacent ferruginous water mass. The transformation from iron formations in the lower part of Member II to the MRBs, was likely caused by a decrease in hydrothermal iron flux and moderate marine oxygenation.

TABLE 1. Major elements and TOC (wt%) of red and green beds from the Xiamaling Formation, Zhaojiashan

TABLE 2. I/(Ca+Mg) ratios and C-O isotope compositions of ankerite concretions in MRBs from Member II of the Xiamaling Formation

TABLE 3. REE+Y (µg/g) of the Xiamaling ankerite concretions

676 **TABLE S1.** Quantitative EDS analysis result of ankerite grains in ankerite concretions

TABLE1. Major elements and TOC (wt%) of red and green beds from the Xiamaling Formation, Zhaojiashan

Sample ID	Lithology	Height (m)	SiO_2	TiO_2	Al_2O_3	TFe_2O_3	MnO	MgO	CaO	Na_2O	K_2O	P_2O_5	LOI	Fe(III)	TOC
1612ZJS-11-01	red shale	6.0	66.83	0.70	13.75	5.25	0.03	2.00	1.06	0.78	3.17	0.27	6.57	3.68	0.17
1612ZJS-11-02	green shale	6.1	66.46	1.03	13.98	5.31	0.03	2.24	0.65	0.35	4.57	0.09	5.66	3.71	0.19
1612ZJS-11-03	red shale	6.2	59.81	0.79	15.21	9.74	0.02	2.29	0.32	0.13	5.09	0.12	5.67	6.82	0.34
1612ZJS-11-04	green shale	6.3	64.09	0.91	15.57	5.41	0.02	2.27	0.77	0.19	5.20	0.12	5.87	3.79	0.27
1612ZJS-11-05	red shale	6.5	60.61	0.75	14.90	8.91	0.04	2.33	1.37	0.19	5.09	0.17	6.14	6.24	0.21
1612ZJS-11-07	green shale	6.8	72.43	1.10	10.01	5.32	0.05	1.91	0.99	0.52	3.26	0.08	4.68	3.72	0.17
1612ZJS-11-08	red shale	6.9	58.24	0.69	14.16	8.55	0.11	2.87	2.33	0.14	4.93	0.13	8.13	5.98	0.37
1612ZJS-11-09	green shale	7.0	69.36	1.05	12.57	4.56	0.03	1.99	0.77	0.47	4.12	0.13	4.98	3.19	0.26
1612ZJS-11-13	red shale	9.2	59.49	0.70	14.52	8.11	0.04	2.37	1.28	0.23	4.83	0.18	7.49	5.68	0.19
1612ZJS-11-14	green shale	9.3	65.21	0.84	13.79	5.10	0.03	2.16	2.04	0.32	4.55	0.12	6.17	3.57	0.21
1612ZJS-11-17	red shale	10.2	61.01	0.68	13.88	8.67	0.05	2.40	1.20	0.16	4.80	0.12	7.31	6.07	0.16
1612ZJS-11-18	green shale	10.3	65.46	0.81	13.32	4.48	0.07	2.34	1.72	0.24	4.52	0.11	6.50	3.14	0.30
1612ZJS-11-19	red shale	10.4	60.97	0.71	14.24	8.75	0.04	2.34	0.85	0.16	4.94	0.15	6.12	6.13	0.37
1612ZJS-11-21	red shale	10.7	62.32	0.69	13.78	7.60	0.04	2.36	1.45	0.14	4.80	0.12	6.09	5.32	0.21
1612ZJS-11-22	green shale	10.8	66.48	0.78	13.71	4.85	0.03	2.15	0.69	0.21	4.68	0.12	5.73	3.39	0.17
1612ZJS-11-25	red shale	11.1	65.22	0.66	14.19	7.19	0.01	2.22	0.75	0.10	4.71	0.09	5.33	5.03	0.20

TABLE 2. I/(Ca+Mg) ratios and C-O isotope compositions of ankerite concretions in red beds from Member II of the Xiamaling Formation

Sample ID	I (μg/g)	Mg (μg/g)	Ca (μg/g)	I/(Ca+Mg) (μmol/mol)	$\delta^{13}C$ (VPDB)‰	$\delta^{18}O$ (VPDB)‰
1612ZJS-11-06	0.14	46282	106202	0.23	-8.3	-9.8
1612ZJS-11-10	0.08	59873	123119	0.11	-7.8	-10.1
1612ZJS-11-11	0.12	57133	131748	0.17	-6.9	-10.5
1612ZJS-11-12	0.10	45215	59141	0.23	-5.7	-9.6
1612ZJS-11-15	0.10	52331	84711	0.19	-6.1	-9.7
1612ZJS-11-16	0.12	62510	156660	0.15	-5.9	-9.7
1612ZJS-11-20	0.10	57418	152448	0.13	-7.1	-10.5
1612ZJS-11-23	0.12	67317	135106	0.15	-7.3	-10.5
1612ZJS-11-24	0.06	58306	129373	0.08	-6.8	-9.1
Min	0.06	45215	59141	0.08	-8.3	-10.5
Max	0.14	67317	156660	0.23	-5.7	-9.1
Average	0.10	56265	119834	0.16	-6.9	-10.0
STDEV	0.02	7225	31623	0.05	0.9	0.5

TABLE 3. REE+Y (μg/g) of the Xiamaling ankerite concretions

Sample ID	La	Ce	Pr	Nd	Sm	Eu	Gd	Tb	Dy	Y	Ho	Er	Tm	Yb	Lu
1612ZJS-11-06	0.976	6.520	1.080	7.390	4.480	1.175	5.661	1.010	5.280	17.700	0.846	1.920	0.229	1.300	0.172
1612ZJS-11-10	1.640	11.100	1.860	13.100	6.580	1.665	8.105	1.400	7.370	28.900	1.170	2.770	0.327	1.970	0.264
1612ZJS-11-11	2.170	11.600	1.810	11.600	5.340	1.181	6.013	0.997	5.030	20.200	0.823	1.870	0.217	1.330	0.187
1612ZJS-11-12	2.450	11.000	1.610	9.930	4.470	1.037	5.205	0.836	4.310	18.000	0.675	1.630	0.184	1.160	0.163
1612ZJS-11-15	2.680	13.100	1.900	11.900	4.830	1.032	4.993	0.817	4.060	16.900	0.686	1.620	0.194	1.210	0.165
1612ZJS-11-16	2.950	11.700	1.590	9.280	3.710	0.872	4.267	0.644	3.330	14.900	0.570	1.320	0.156	1.050	0.130
1612ZJS-11-20	3.340	15.700	2.280	14.700	5.710	1.388	6.395	1.010	5.060	21.600	0.832	1.990	0.226	1.420	0.183
1612ZJS-11-23	2.720	13.100	1.930	12.600	5.620	1.277	6.018	0.960	5.170	21.200	0.827	1.940	0.228	1.380	0.184
1612ZJS-11-24	0.289	1.390	0.231	1.630	0.819	0.208	0.762	0.111	0.553	1.870	0.092	0.246	0.030	0.225	0.027

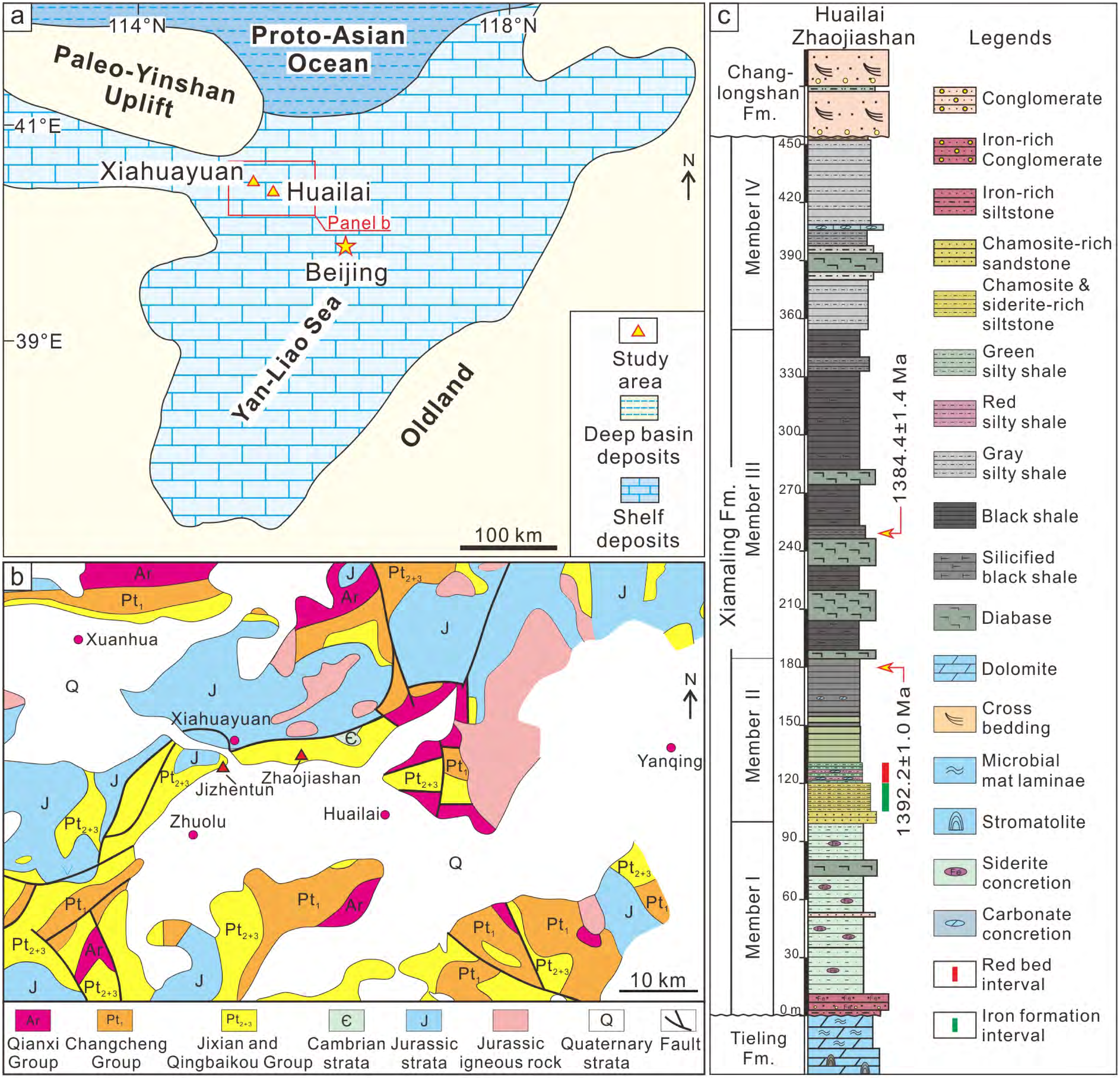
a
114°N
118°N
Proto-Asian Ocean
Paleo-Yinshan Uplift
41°E
39°E
Xiahuayuan
Huailai
Panel b
Beijing
Yan-Liao Sea
Oldland
N
Study area
Deep basin deposits
Shelf deposits
100 km
b
Ar
Pt1
Pt2+3
J
Q
Є
Xuanhua
Xiahuayuan
Jizhentun
Zhaojiashan
Zhuolu
Huailai
Yanqing
N
10 km
Qianxi Group
Changcheng Group
Jixian and Qingbaikou Group
Cambrian strata
Jurassic strata
Jurassic igneous rock
Quaternary strata
Fault
c
Huailai Zhaojiashan
Changlongshan Fm.
Xiamaling Fm.
Member IV
Member III
Member II
Member I
Tieling Fm.
450
420
390
360
330
300
270
240
210
180
150
120
90
60
30
0 m
1384.4±1.4 Ma
1392.2±1.0 Ma
Legends
Conglomerate
Iron-rich Conglomerate
Iron-rich siltstone
Chamosite-rich sandstone
Chamosite & siderite-rich siltstone
Green silty shale
Red silty shale
Gray silty shale
Black shale
Silicified black shale
Diabase
Dolomite
Cross bedding
Microbial mat laminae
Stromatolite
Siderite concretion
Carbonate concretion
Red bed interval
Iron formation interval

Figure 1

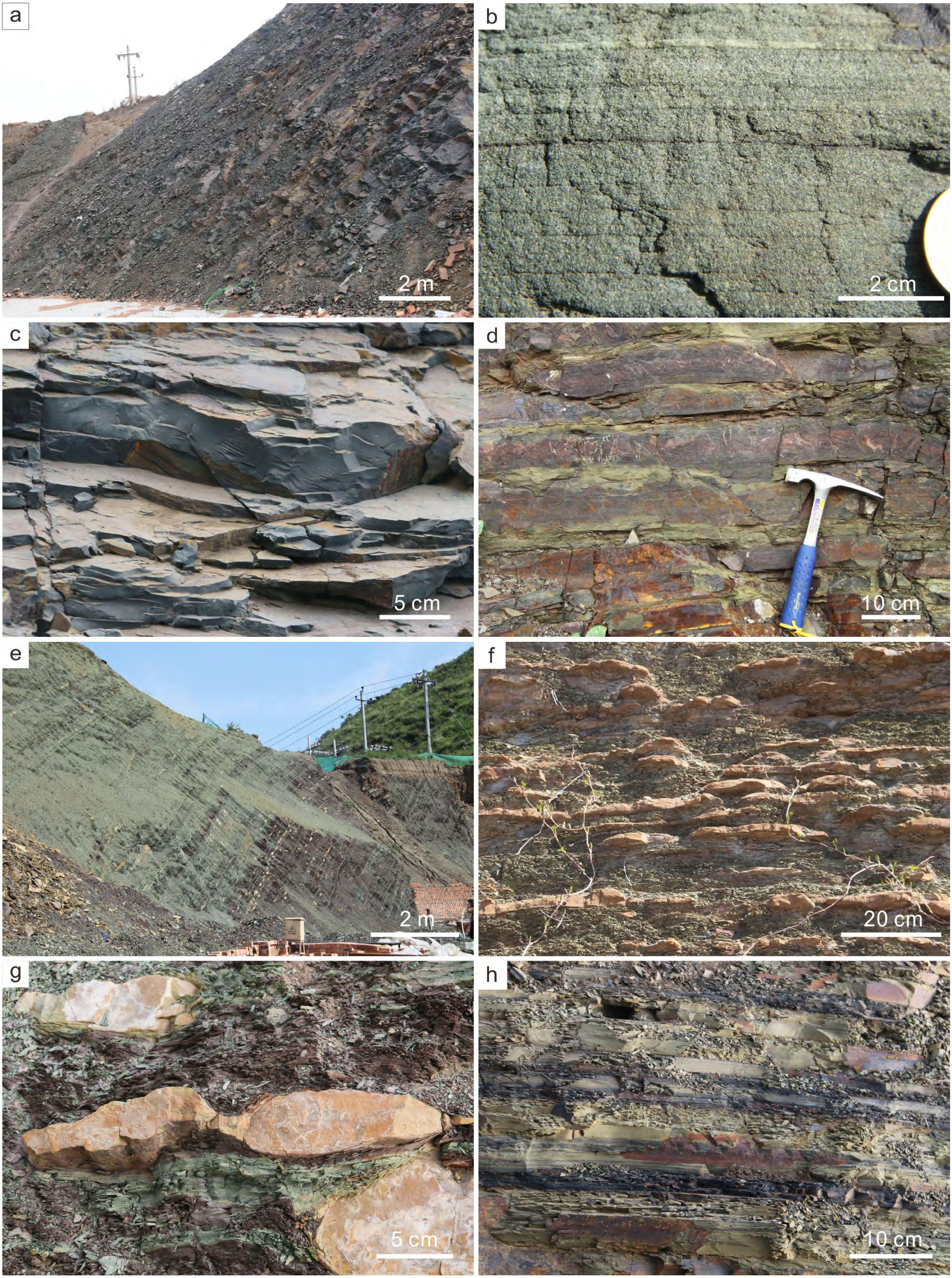

Figure 2

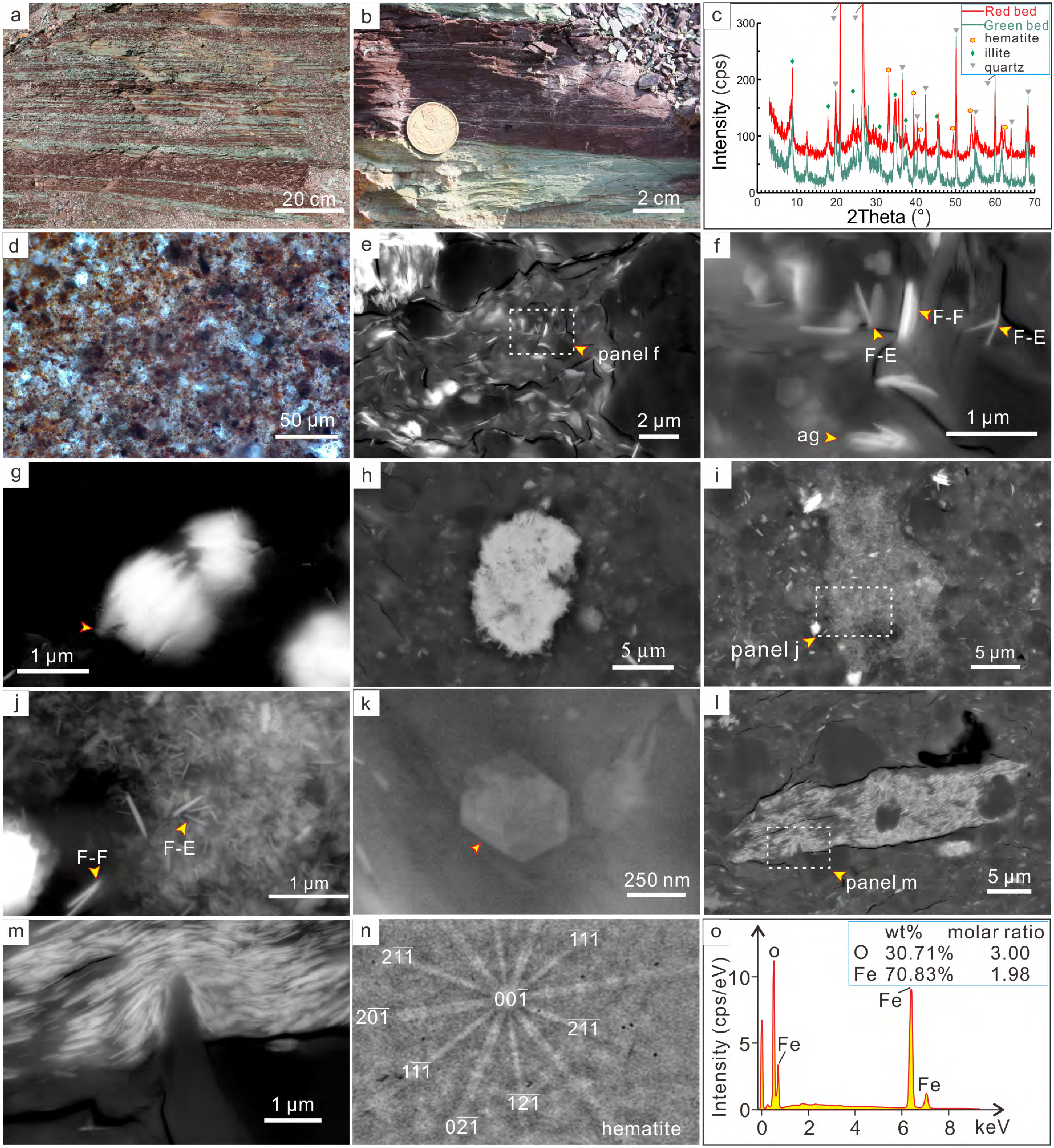
a
20 cm
b
2 cm
c
Red bed
Green bed
hematite
illite
quartz
Intensity (cps)
0
100
200
300
2Theta (°)
0
10
20
30
40
50
60
70
d
50 μm
e
panel f
2 μm
f
F-F
F-E
F-E
F-E
ag
1 μm
g
1 μm
h
5 μm
i
panel j
5 μm
j
F-F
F-E
1 μm
k
250 nm
l
panel m
5 μm
m
1 μm
n
$2\bar{1}\bar{1}$
$\bar{1}1\bar{1}$
$00\bar{1}$
$20\bar{1}$
$\bar{2}\bar{1}\bar{1}$
$1\bar{1}\bar{1}$
$\bar{1}\bar{2}\bar{1}$
$0\bar{2}\bar{1}$
hematite
o
wt%
molar ratio
O 30.71% 3.00
Fe 70.83% 1.98
O
Fe
Fe
Fe
Intensity (cps/eV)
0
5
10
0
2
4
6
8
keV

Figure 3

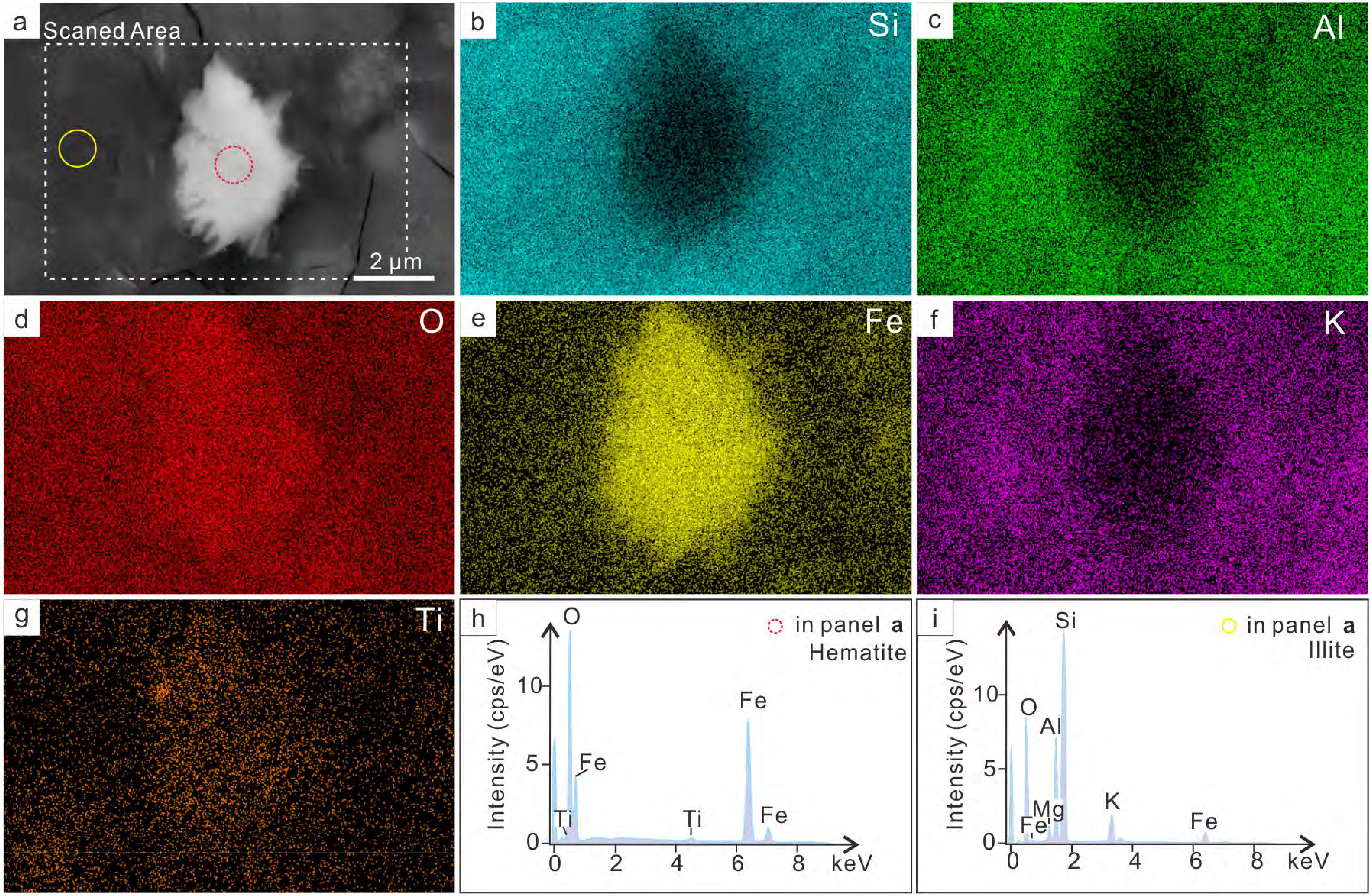
a
Scaned Area
2 μm
b
Si
c
Al
d
O
e
Fe
f
K
g
Ti
h
in panel a
Hematite
Intensity (cps/eV)
O
Fe
Ti
Ti
Fe
Fe
0
5
10
0
2
4
6
8
keV
i
in panel a
Illite
Intensity (cps/eV)
Si
O
Al
Mg
Fe
K
Fe
0
5
10
0
2
4
6
8
keV

Figure 4

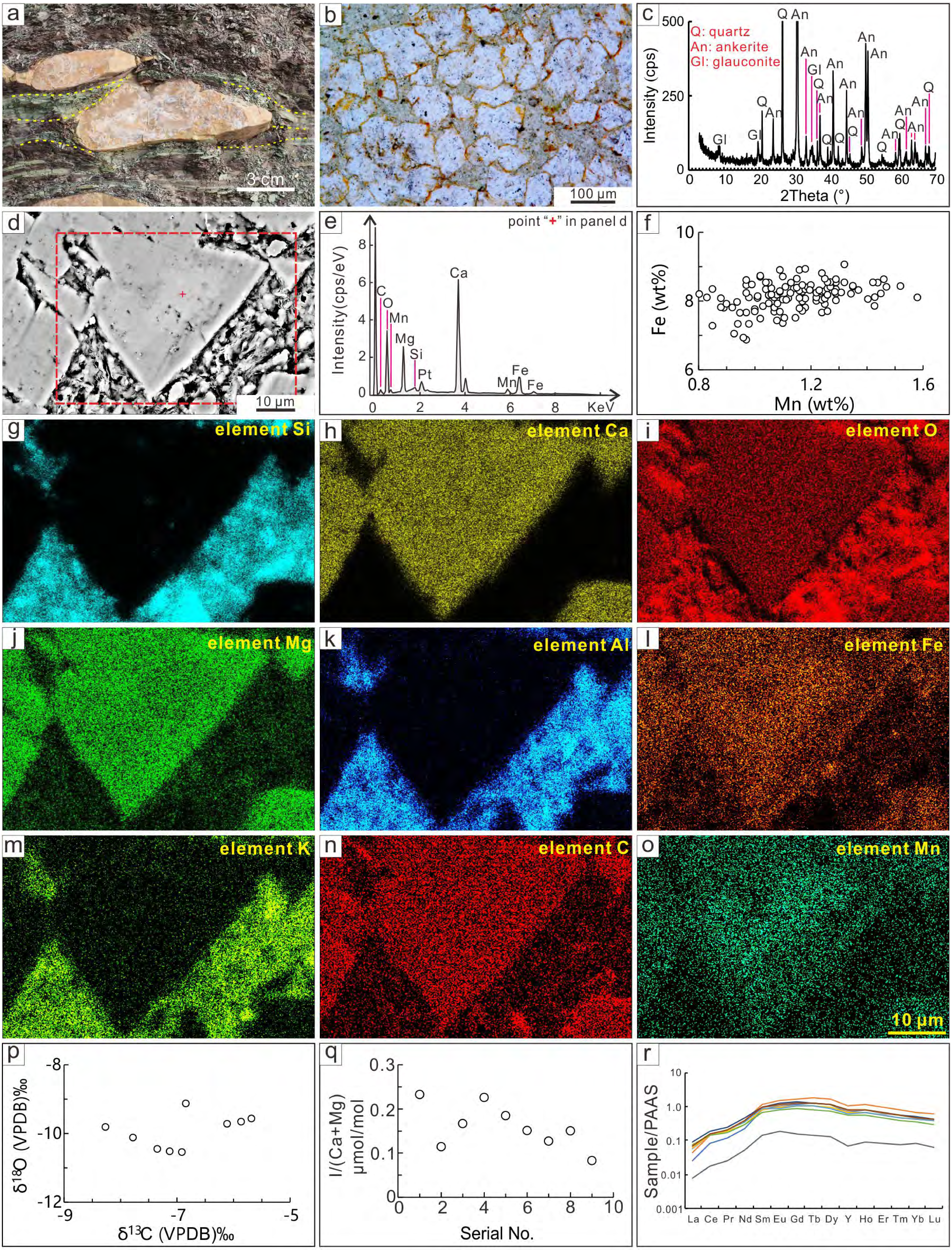
a
3 cm
b
100 μm
c
Q: quartz
An: ankerite
Gl: glauconite
Intensity (cps)
2Theta (°)
Q
An
Gl
d
10 μm
e
point "+" in panel d
Intensity(cps/eV)
KeV
C
O
Mn
Mg
Si
Pt
Ca
Fe
f
Fe (wt%)
Mn (wt%)
g
element Si
h
element Ca
i
element O
j
element Mg
k
element Al
l
element Fe
m
element K
n
element C
o
element Mn
10 μm
p
δ18O (VPDB)‰
δ13C (VPDB)‰
q
I/(Ca+Mg) μmol/mol
Serial No.
r
Sample/PAAS
La Ce Pr Nd Sm Eu Gd Tb Dy Y Ho Er Tm Yb Lu

Figure 5

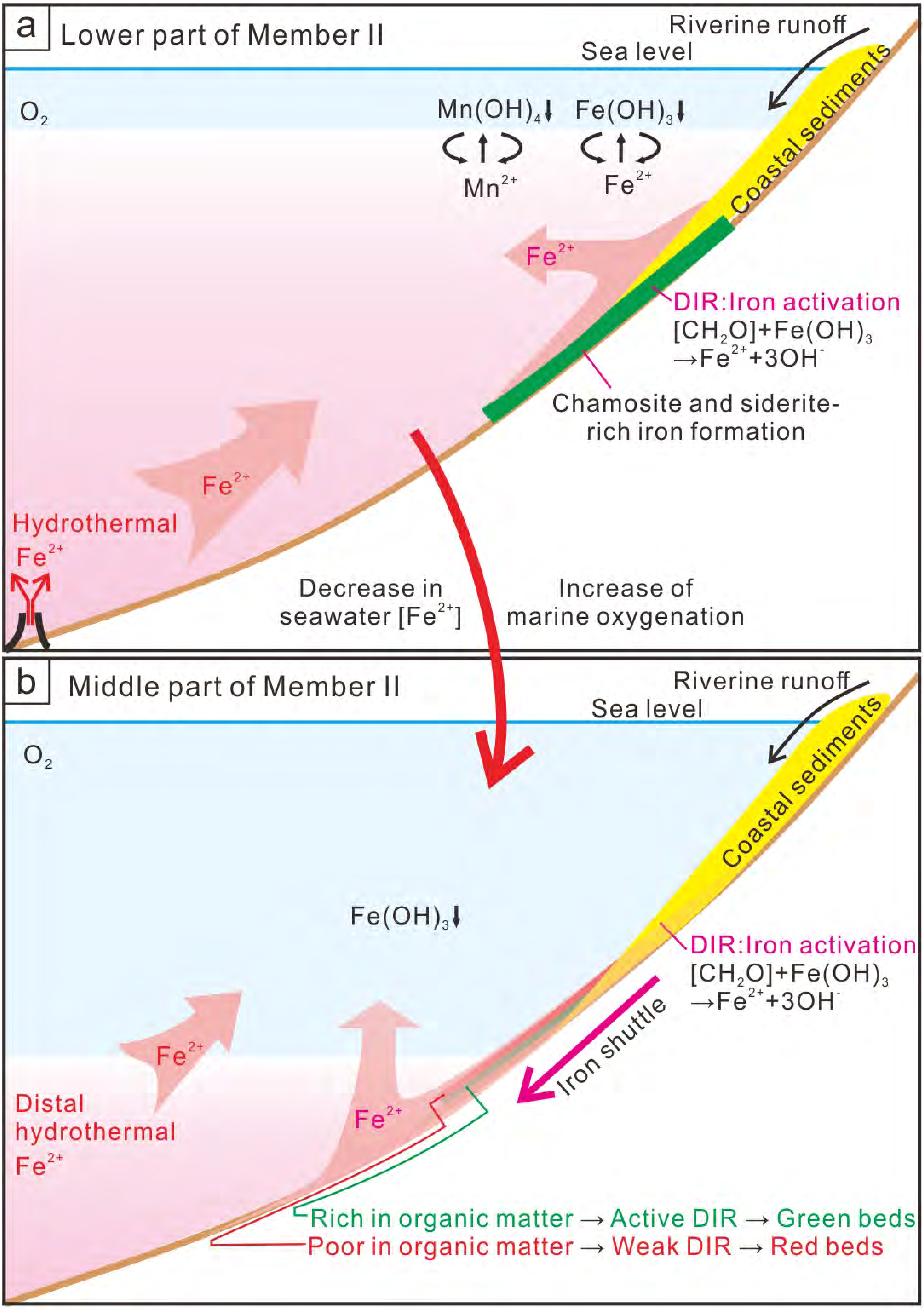
a
Lower part of Member II
Riverine runoff
Sea level
Coastal sediments
O₂
Mn(OH)₄
Fe(OH)₃
Mn²⁺
Fe²⁺
Fe²⁺
DIR:Iron activation
[CH₂O]+Fe(OH)₃ →Fe²⁺+3OH⁻
Chamosite and siderite-rich iron formation
Fe²⁺
Hydrothermal Fe²⁺
Decrease in seawater [Fe²⁺]
Increase of marine oxygenation
b
Middle part of Member II
Riverine runoff
Sea level
Coastal sediments
O₂
Fe(OH)₃
DIR:Iron activation
[CH₂O]+Fe(OH)₃ →Fe²⁺+3OH⁻
Iron shuttle
Fe²⁺
Distal hydrothermal Fe²⁺
Fe²⁺
Rich in organic matter → Active DIR → Green beds
Poor in organic matter → Weak DIR → Red beds

Figure 6